It may be possible to estimate the antitumor effect and normal tissue response based on the microdistribution and concentration of ^{10}B compound in tissues, because the effect of each particle is limited to the reaction site. To confirm this possibility, many samples should be treated for screening of the potency of the boron compound. Thus, it is desirable that a rapid and simple method for estimating the boron compound effect be established, and that preparation of the sample section is also quick and straightforward.

The effect of the boron compound is dependent on the microdistribution of ^{10}B in the cell nucleus. Therefore, it is important to identify the labeled cell nucleus and the position of the ^{10}B atom at the submicron scale.

Much effort has been devoted to visualizing the ^{10}B microdistribution, one of the methods employed being an alpha-autoradiography technique [5–8]. However, the range of BNCT particles is too great to allow precise localization of ^{10}B atoms in cells and tissues. An alpha particle with the range of 8 μm in cell is isotropically emitted by the ^{10}B(n,α)^{7}Li reaction. The maximum deviation from the reaction point to detection point is around 8 μm using the general alpha autoradiography method, which is too large to identity the ^{10}B distribution in cell. Several proposals have been made on how to resolve this defect. Amemiya *et al.* irradiated the cells on the CR-39 solid state track detector with soft X-rays, and used atomic force microscopy (AFM) to observe the cell images and an extremely tiny pit of the alpha particle track made by soft X-rays and by the ^{10}B(n, α)^{7}Li reaction, respectively [9]. The role of soft X-rays is to distinguish changes in the bulk etch rate and in the sensitivity of CR-39. A high-resolution atomic force microscope was required to observe the very faint cell image induced by soft X-rays that could not be resolved by an optical microscope.

Amemiya *et al.* and Konishi *et al.* also published special techniques using UV light to record cellular images directly on to the surface of CR-39. Amemiya *et al.* established a superior method for high-resolution neutron-induced alpha autoradiography using CR-39 and an AFM [10]. This technique can also detect the 3D image of an etched pit in order to measure the incident angle of the charged particle. However, in order to prepare the section with a thickness of 1 μm, the tissue is fixed by glutaraldehyde and osmium tetroxide, dehydrated and then embedded in epoxy resin. Many processes and much time are needed for the preparation of the sample. Furthermore, there is a significant amount of activation of samples by the irradiation of thermal neutrons while the irradiated samples are being taken from the thermal neutron irradiation facility to the AFM facility. It is difficult to rapidly and simply treat many samples of tissue containing ^{10}B atoms using this technique, because of the need for complicated preparation of the tissue section and special devices such as an AFM. However, if very precise information on the distribution of ^{10}B in tissue is needed, this technique should be applied.

Konishi *et al.* extended the method developed by Amemiya *et al.* for estimation of the incident position of the charged particle [11]. Furthermore, Konishi *et al.* also showed the superimposed image of etched pits and cellular images directly onto the surface of CR-39 exposed by the UV light using the conventional optical microscope. However, they mentioned that the contours of the cell nuclei were difficult to identify because of the similar UV absorption of the nuclei and the cytoplasm. Furthermore, they mentioned that there are hardly visible etched pits on the cell relieves because of uneven enhancement of the etching velocity due to UV exposure during the cell image-transferring procedure.

In another study, Solares *et al.* developed a unit of silica glass/tissue sample/Ixan/Lexan, and implemented a technique that does not create a relative gap between the tissue and the pit on the track detector generated by the ^{10}B(n, α)^{7}Li reaction. In that study, a general microscope was suitable as an observation instrument [12]. However, a technique for preparation of a special track detector was needed before the examination could be performed.

It is desirable that a clear image of the cellular nucleus and etched pits is obtained for evaluation of the effect of the boron compound used in BNCT at the submicron scale. It is also necessary to obtain a superimposed image of the fluorescently stained cell nucleus image and the etched pits. The purpose of this manuscript is the development of the alpha-autoradiography with position resolution at submicron level.

In the present work, we report on an improved method that allows simple and precise estimation of ^{10}B microdistribution using commercially available tools, such as a CR-39 solid-state track detector, an optical microscope, or a fluorescence microscope. The CR-39 is widely used as a neutron solid-state track detector for a personal dosimeter. In order to improve the position resolution of ^{10}B distribution, we devised a novel method using the circularity of the shape of the etched pits, and we performed a verification test as proof of principle for our improved method. Moreover, in order to acquire an image without a relative gap in the etched pit on a CR-39 and tissue image, we propose an improved superposition method that uses the mark on a CR-39 as a standard that is not eliminated by the etching process. As a reliability test for this technique, we present an image of the intracellular microdistribution of ^{10}B using a tissue sample from the brain of a mouse injected with 500 mg/kg of BPA.

MATERIALS AND METHODS

High-resolution analysis of etched pits using their circularity

CR-39 plastic track detectors of BARYOTRAK (Nagase Landauer, Ltd, Japan) were used. In alpha-autoradiography, a several micron thick tissue sample containing the ^{10}B

atoms is installed on a CR-39, and damaged polymer chains are formed in the CR-39 by alpha particles and lithium nuclei that are emitted following the ^{10}B(n, α)^{7}Li reaction triggered by thermal neutron irradiation. Etched pits corresponding to the position of the incident charged particles are formed by using chemical etching of the CR-39 to microscopically expose the damage tracks.

Figure 1 schematically shows the layout that describes etched pit quantities of track formation at a constant etched rate. The direction at which the charged particle enters can be determined by observing the shape of an etched pit. Because the tissue sample has a non-negligible thickness, the emission point of the particles that enter aslant differs from the position of the etched pit on the CR-39. Moreover, the shape of the etched pit becomes ellipse-like. On the other hand, if the charged particle enters the CR-39 perpendicularly, the etched pit will be a true circle and the deviation will be zero (Fig. 1).

Therefore, an etched pit with needs to have the shape of a true circle on the CR-39 in order to correctly identify the location of the ^{10}B(n, α)^{7}Li reaction. However, the absolute number of pits will be lower if only true circle pits are counted. Instead, a small deviation should be permitted in the actual analysis. The circularity of the etched pits is derived from a digitized image giving the area and the boundary length of each etched pit. Circularity is defined by the following formula:

$$C = 4\pi S/L^2 \qquad (1)$$

In Equation (1), S and L are the area and the boundary length of an etched pit, respectively. A true circle is assumed when circularity approaches the value of 1.

To estimate the relationship between the circularity and the minor-to-major axis ratio, the area S and the boundary
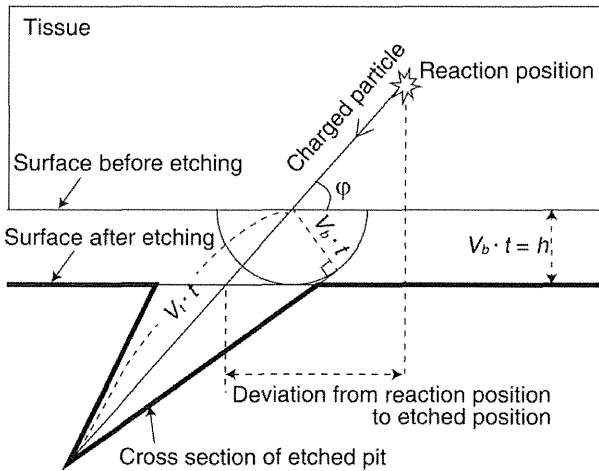
length L are given by the following equations:

$$S = \pi ab, L = 4aE(k), k^2 = 1 - (b^2/a^2),$$
$$E(k) = \int_0^{\pi/2} \sqrt{1 - k^2\sin^2\theta}\,d\theta \qquad (2)$$

In the above equations, $E(k)$ is an elliptic integral of the second kind. The quantities a and b are the major axis and the minor axis, respectively. The circularity C is then given by:

$$C = 4\pi^2(b/a)/(4E(k))^2 \qquad (3)$$

Figure 2 shows the relationship between the circularity and the minor-to-major axis ratio of an etched pit.

On the other hand, the major and the minor axis of an etched pit are given by the following equations [13]:

$$a = 2h\frac{\sqrt{V^2 - 1}}{V\sin\varphi + 1} \qquad b = 2h\sqrt{\frac{V\sin\varphi - 1}{V\sin\varphi + 1}}, \qquad (4)$$

where h, V, and ϕ are the surface removal, the track to bulk etch rate ratio (Vt/Vb), and the angle at which the particles are incident on the surface of CR-39. To estimate the deviation from the reaction point to the etched position, the relationship between ϕ and the minor-to-major axis ratio is given, using Equation (4), by the following equation:

$$\sin\varphi = \sqrt{\frac{\frac{b^2}{a^2}(V^2 - 1) + 1}{V^2}} \qquad (5)$$

Figure 2 also shows the relationship between the angle ϕ and the minor-to-major axis ratio. In [14], the value of V and h were 7 and 1.2 µm, respectively, for alpha particles incident under the etching conditions of 6N NaOH at a temperature of 70°C for 1 h.

Fig. 1. Schematic presentation to describe the etched pit quantities of track formation at a constant etch rate.
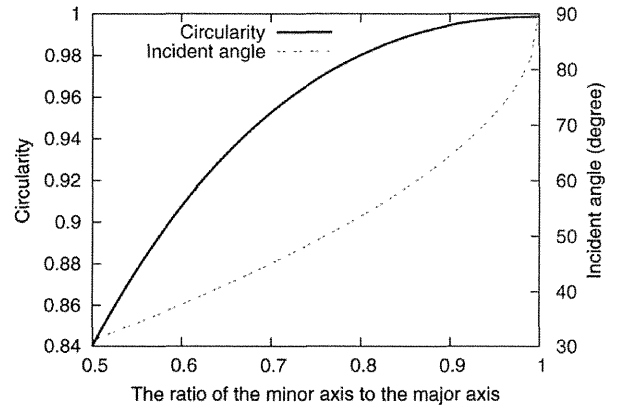

Fig. 2. The relationship between the circularity and the minor-to-major axis ratio of an etched pit.

The minor-to-major axis ratio is estimated to be 0.95 for an etched pit with a circularity of 0.995. If the selected value of circularity ranges between 0.995 and 1, the maximal deviation of the etched pit position on CR-39 from the location of $^{10}B(n, \alpha)^{7}Li$ reaction in the tissue sample is within 1.7 μm.

In order to confirm that the value of the circularity of the etched pit induced by the perpendicularly incident charged particle approaches 1, we irradiated the samples with thermal neutrons for 1 and 5 min. The irradiated samples had a predefined concentration of BPA mounted on quartz glass, and a 1–3 μm thick thin mylar foil (provided by Goodfellow Cambridge Ltd, Japan) was sandwiched between the samples and the CR-39. Furthermore, a sample without mylar foil was also prepared. In all, four types of samples were prepared. The irradiation was performed using the pneumatic tube of the thermal column at the Kyoto University Research Reactor Institute (KUR) [15]. KUR is a light-water moderated tank-type reactor operated at a thermal power of 1 MW or 5 MW. Thermal neutron flux is 8×10^{10} (n/cm^{2}s) while operating at 1 MW.

Following irradiation, the tracks on CR-39 were chemically etched using 6N NaOH at a temperature of 70°C for 1 h. The etched CR-39 was examined using an optical microscope, and images of the etched pits were acquired. The acquired images of the etched pits were digitized, and for every etched pit the circularity was derived from the area and boundary length.

Method of superposition of the cell image and the etched pits

In alpha-autoradiography, the chemical etching process does not allow a tissue sample to remain in the image of an etched pit. Therefore, reference points are necessary in order to superimpose a tissue sample and etched pit images. The reference points must be observable both on the tissue sample and on the etched pit images; thus, we devised a method of making a scratch of two cross-lines on the CR-39, each line being several microns wide. Making cross-lines was necessary in order to determine the position in two dimensions.

Figure 3 shows the schematic layout of the superposition technique. The tissue sample is first stained with a Hoechst in order to obtain an image of the cell nucleus; images of the tissue sample with scratched cross-like reference points are acquired in both the bright and fluorescence fields at low and high magnifications. Low magnification is × 40–200, selected according to the scratched position, and high magnification is × 200–400. The resolution for magnification of × 200 corresponds to 0.5 μm/pixel. The image was obtained using the commercially available optical microscope, BZ-9000 (Keyence, Japan). This microscope can join the high magnification images into one image of a wide range by scanning the microstage.

The high-to-low magnification image relation of the area of interest is then recorded based on the two images. After
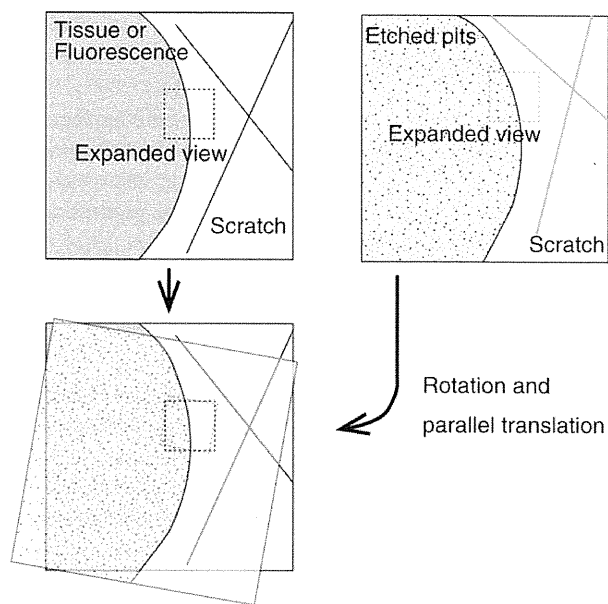

Fig. 3. Schematic of the layout for the method of superposition of the fluorescence and/or the bright-field image of the tissue with the CR-39 etched-pit image.

carrying out the chemical etching, the process of monitoring and recording images of the etched pits is repeated. In the next step, images of a tissue sample and of an etched pit are superimposed by parallel translation and rotation, so that the center of the after- and before- etching line are in agreement with both low magnification images. The amount of parallel translation and the angle in this superposition are recorded. The center of the after-etching line will be the superimposed on the before-etching line because the scratch is uniformly etched. Furthermore, the image of the cross-like scratch can be matched to within microns because the pixel size is 0.5 μm. However, if a higher resolution image were to be obtained, we should apply the superposition method developed by Amemiya *et al.* and Konishi *et al.* using UV light to record cellular images directly on to the surface of the CR-39.

In order to superimpose the images at high magnification, first, two low-magnification images of the bright and fluorescence fields and etched pits are matched in the area of interest. Then, two high-magnification images are also matched, using the amount of parallel translation and the angle of rotation that were recorded above.

To confirm the validity of the superposition technique, a sample tissue image was acquired from a frozen 4-μm thick section from the brain of a mouse that had been injected with 500 mg/kg of BPA. The tissue sample was frozen with liquid nitrogen, and the frozen section was made by microtome. The frozen section thickness 4 μm was mounted on the CR-39. C3H/He male mice of 10 weeks old were used for experiments. The portion of brain used was the left brain.

The frozen section was installed on the CR-39 with scratched reference points, and neutron irradiation was performed for 5 min using the thermal column of the KUR.

After irradiation, fluorescence staining of the nucleus was carried out using Hoechst, and both low and high magnification images were acquired. Chemical etching and image observation was carried out following the same process as the one that was described above.

RESULTS

Image processing of the etched pit using circularity

The images of etched pits are shown in Fig. 4 for different mylar thicknesses, ranging from 0 to 3 μm in steps of 1 μm. To prevent the overlap of etched pits, the irradiation time with thermal neutrons was set to 1 or 5 min, corresponding to fluencies of 4.8×10^{12} and 2.4×10^{13} (cm^{-2}) for mylar thicknesses of 0, 1, 2 and 3 μm, respectively, under a ^{10}B concentration of 2.5 ppm.

Because an incident particle that enters aslant is stopped within the mylar, it was found that the relative frequency of incident particles that enter perpendicularly increases with increasing mylar thickness.

Moreover, because the energy deposit of the lithium nuclei and alpha rays emitted by the ^{10}B(n, α)^{7}Li reaction decreased with increasing thickness of the mylar, it was observed that the size of the etched pit became smaller.

Figure 5 presents the relationship between the thickness of the mylar and the number of etched pits that were induced in the visual field of 1.1×10^{4} μm^{2} in 1 min of neutron irradiation, corresponding to 4.8×10^{4} n/ μm^{2}, at 1 ppm of ^{10}B. The number of measured etched pits in the area of 1.1×10^{4} μm^{2} without the mylar was 180 pits/ppm/min, corresponding to a detection efficiency of 3.4×10^{-7} pits/ppm/neutron.

Further, we performed simulations of the experimental layout using the heavy particle transportation code of PHITS [16]. The results of these simulations using PHITS were in good agreement with the experimental results. According to the simulation results, the ratios of alpha particle events to total events were 78, 90 and 99% for mylar thicknesses of 1, 2 and 3 μm, respectively, because the range of alpha particles was larger than that of ^{7}Li nuclei.

Image processing was carried out to quantify the characteristics of the etched pits. The relationship between the average area (or the circularity of an etched pit) and the mylar thickness is shown in Fig. 6. It was found that the area of a pit becomes small and the average circularity approaches 1 with increasing mylar thickness. It was also found that, for perpendicularly incident particles, the relative number of etched pits increases with increasing mylar thickness.
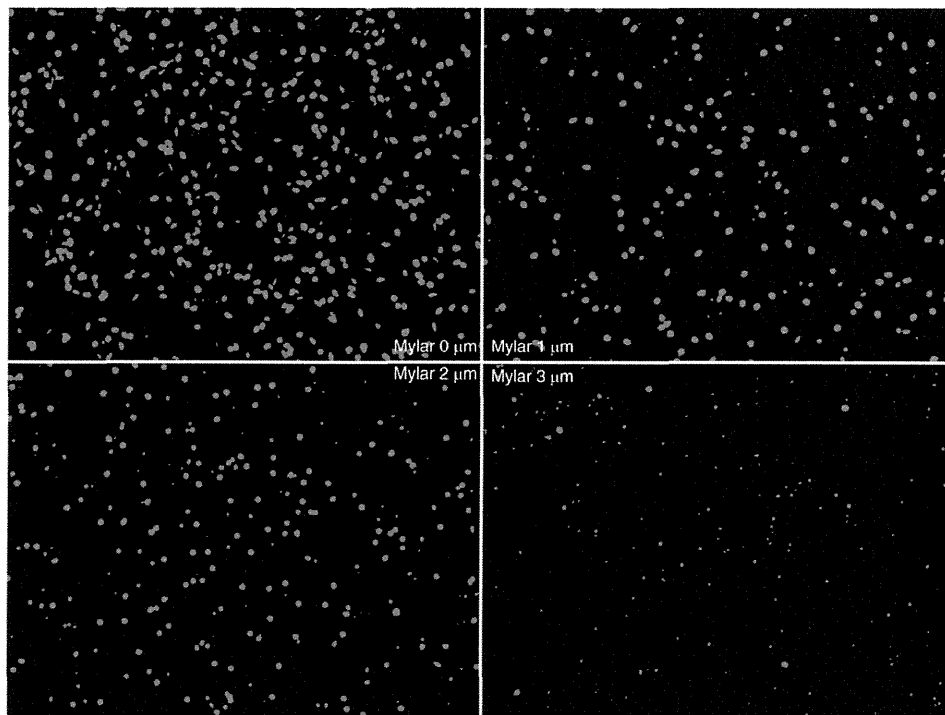

Fig. 4. Images (×400) of etched pits on the CR-39 obtained for mylar thickness values ranging from 0 to 3 μm.
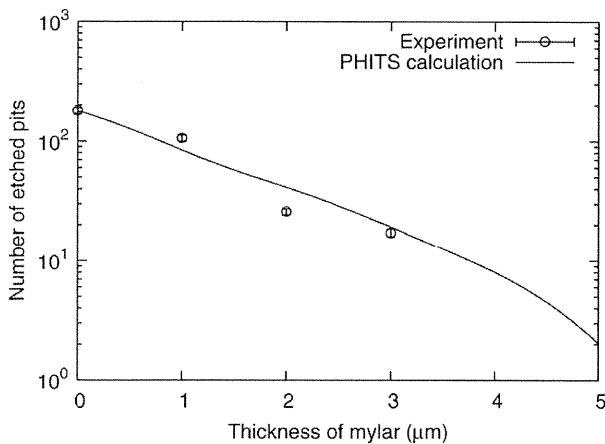
Fig. 5. Relationship between mylar thickness and the number of etched pits per 1 ppm, for a 1 min long irradiation. The solid line shows the results of calculations obtained using the PHITS code. The maximum error for the experimental data was 6.8%.
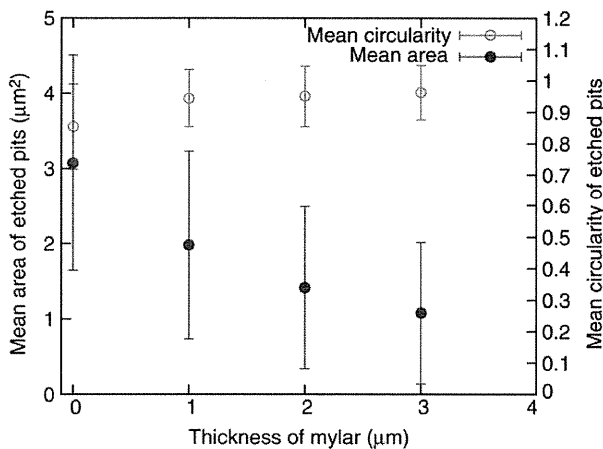

Fig. 6. Relationship between the average area or the circularity of an etched pit and mylar thickness. The error for the area is large because the area size is dependent on the incident energy and the angle of incidence of the charged particles.

Superposition of a tissue sample and an etched-pit image

Figure 7 shows a bright-field and a fluorochromic image for a tissue sample, as well as a low-magnification etched-pit image. No misalignment exists between the bright and a fluorescence images, because the bright and a fluorescence images were obtained by only changing the lens of the microscope. Next, an area of interest was selected in the low-magnification image that was also recorded in the high magnification image.

Only etched pits with circularity ranging between 0.995 and 1 were selected to obtain the 'perpendicularly incident' particles. Moreover, in order to superimpose an image of an
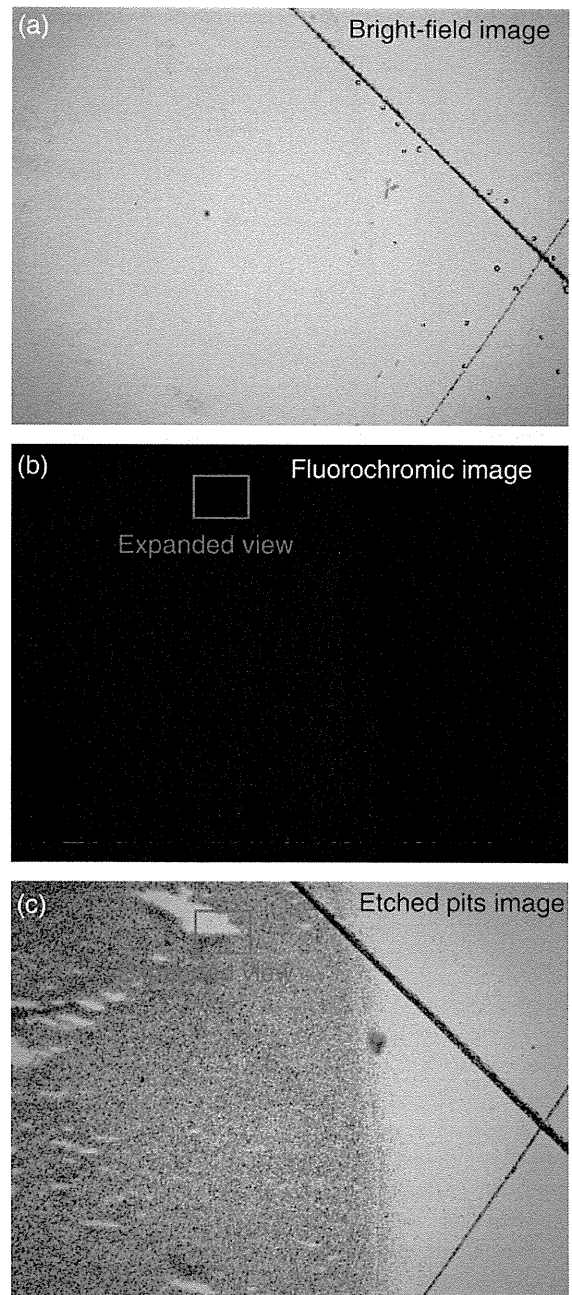

Fig. 7. (a) An optical bright-field microscope image of a tissue sample, (b) a fluorescence image of the same tissue sample, and (c) a low magnification image (×100) of the etched CR-39 showing a multitude of pits.

etched pit on a fluorescence image, the image was moved based on the information on the amount of parallel translation and the angle of rotation. The superimposed image is shown in Fig. 8. Red dots show the etched pits chosen, i.e. circularity from 0.995 to 1. The locations of the red dots correspond to the locations of $^{10}B(n, \alpha)^7Li$ reactions.

Fig. 8. Zoomed-in section of images in Fig. 7 (b–c), superimposed to show the pit position (red) and the mouse brain showing the left hemisphere cell nuclei injected with 500 mg/kg of BPA (blue). BPA is an amino-acid analog and localized in the cell because of the enhancement of transport of an amino acid.

Because cell nuclei were clearly identified in the fluorescence image, the relationship of the sites of ^{10}B to cell nuclei, i.e. the microdistribution of ^{10}B in cells or tissue, was precisely determined by the superimposed fluorescence and etched pit images of high magnification. Our new method is expected to become useful for predicting the BNCT effects of new ^{10}B compounds.

DISCUSSION

In this research, we developed a new method that allows simple and precise determination of the intracellular microdistribution of ^{10}B using commercially available devices such as a CR-39 solid state track detector, a commercially available optical microscope, or a fluorescence microscope. Aiming at improving the position resolution of ^{10}B microdistribution, the principle of this technique was confirmed using information on the circularity of etched pits, and a proof-of-principle test was performed. In this article, the range of circularity was selected to be from 0.995 to 1, corresponding to a maximal deviation of 1.7 μm, allowing us to obtain a sufficient number of events. If the CR-39 can detect lithium nuclei, whose range is shorter than that of alpha particles, the maximal deviation will be < 1 μm. Because alpha particles and lithium nuclei are emitted in opposite directions, half of the events in the ^{10}B(n, α)^{7}Li reaction are caused by the incidence of lithium nuclei. Furthermore, the deviation becomes smaller if the reaction occurs in the proximity of the CR-39.

Using the proposed method, we observed superposition pictures of ^{10}B microdistribution not obtainable by normal alpha-autoradiography. For example, the superposition
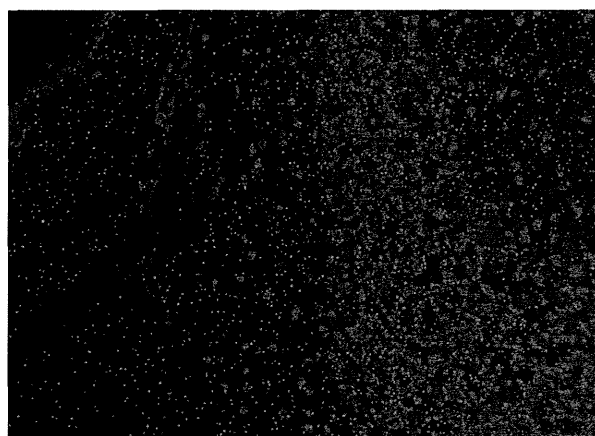

Fig. 9. Superimposed images (×200) of a mouse brain injected with 500 mg/kg of BPA and etched CR-39, showing pits outside of cells.

picture of a brain surface is shown in Fig. 9. Many etched pits were observed at places where cells were not present. This can be explained as follows. When a frozen section is created, blood that adheres to the brain surface may penetrate into the crevice of brain surfaces. When blood is observed outside the tissue, its etched-pit images may serve as a standard for an estimation of the ^{10}B concentration within the tissue or cells if the ^{10}B concentration in the blood is known [17, 18]. It is important to consider the saturation point of etched pits for our technique. Gaillard et al. described the occurrence of saturation as a function of incident particle fluence and etched pit size. They showed that the fluence of 1×10^8 (pits/cm^2) can be counted without saturation for a pit diameter of ~ 1 μm. According to our results, described in *Image processing of the etched pit using circularity*, the number of measured etched pits in an area of 1.1×10^4 (μm^2) was 180 (pits/ppm/min), corresponding to 1.6×10^6 (pits/ppm/min/cm^2). If the irradiation time is 1 min, for a boron concentration of up to 61 ppm the sample is not saturated.

A performance test was also performed, and a superposition image was successfully obtained without a significant gap. However, to obtain higher resolution images with submicron deviation, the frozen section of tissue sample should be thinner with selected pit circularity approaching 1 and a shorter etching time to reduce the surface removal.

In future work, our newly developed method will be applied in evaluation tests for new borated compounds of BNCT.

FUNDING

REFERENCES

1. Barth RF, Coderre JA, Vicente MG *et al.* Boron neutron capture therapy of cancer: current status and future prospects. *Clin Cancer Res* 2005;**11**:3987–4002.
2. Coderre JA, Turcotte JC, Riley KJ. Boron neutron capture therapy: cellular targeting of high linear energy transfer radiation. *Technol Cancer Res Treat* 2003;**2**:355–75.
3. Mishima Y, Honda C, Ichihashi M *et al.* Treatment of malignant melanoma by single thermal neutron capture therapy with melanoma-seeking ^{10}B-compound. *Lancet* 1989;**2**:388–9.
4. Haselsberger K, Radner H, Pendl G. Boron neutron capture therapy: boron biodistribution and pharmacokinetics of $Na_2B_{12}H_{11}SH$ in patients with glioblastoma. *Cancer Res* 1994;**54**: 6318–20.
5. Altieri S, Bortolussi S, Bruschi P *et al.* Neutron autoradiography imaging of selective boron uptake in human metastatic tumours. *Appl Radiat Isot* 2008;**66**:1850–5.
6. Andrea W, Jean M, Raymond M *et al.* Boron analysis and boron imaging in biological materials for Boron Neutron Capture Therapy (BNCT). *Crit Rev Oncol Hematol* 2008;**68**:66–90.
7. Ogura K, Yamazaki A, Yanagie H *et al.* Neutron capture autoradiography for a study on boron neutron capture therapy. *Radiat Meas* 2001;**34**:555–8.
8. Ceberg CP, Salford LG, Brun A. Neutron capture imaging of 10B in tissue specimens *Radiother Oncol* 1993;**26**:139–46.
9. Amemiya K, Takahashi H, Nakazawa M *et al.* Soft X-ray imaging using CR-39 plastics with AFM readout. *Nucl Instrum Meth Phys Res B* 2002;**187**:361–6.
10. Amemiya K, Takahashi H, Kajimoto Y *et al.* High-resolution nuclear track mapping in detailed cellular histology using CR-39 with the contact microscopy technique. *Radiat Meas* 2005;**40**:283–8.
11. Konishi T, Amemiya K, Natsume T *et al.* A new method for the simultaneous detection of mammalian cells and ion tracks on a surface of CR-39. *J Radiat Res* 2007;**48**:255–61.
12. Solares GR, Zamenhof RG. A novel approach to the microdosimetry of neutron capture therapy. Part I. High-resolution quantitative autoradiography applied to microdosimetry in neutron capture therapy. *Radiat Res* 1995;**144**:50–8.
13. Somogyi G. Development of etched nuclear tracks. *Nuclear Instrum Meth Phys Res* 1980;**173**:21–42.
14. Green P, Ramli S, Najjar F *et al.* A study of bulk-etch rates and track-etch rates in CR39. *Nucl Instrum Meth Phys Res* 1982;**203**:551–9.
15. Kyoto University Research Reactor Institute. http://www.rri.kyoto-u.ac.jp/en/facilities/kur (9 August 2013, date last accessed).
16. Niita K, Sato T, Iwase H *et al.* PHITS – a particle and heavy ion transport code system. *Radiat Meas* 2006;**41**: 1080–90.
17. Woollard JE, Blue TE, Curran JF. An alpha autoradiografic technique for determination of ^{10}B concentrations in blood and tissue. *Nucl Instrum Meth Phys Res A* 1990;**299**:600–5.
18. Gadan MA, Bortolussi S, Postuma I *et al.* Set-up and calibration of a method to measure ^{10}B concentration in biological samples by neutron autoradiography. *Nucl Instrum Meth Phys Res B* 2012;**274**:51–6.

CASE REPORT

Administration of gefitinib via nasogastric tube effectively improved the performance status of a patient with lung adenocarcinoma-derived meningeal carcinomatosis

Takeshi Okuda · Hidetoshi Hayashi · Mitsugu Fujita · Hiromasa Yoshioka ·
Takayuki Tasaki · Kazuhiko Nakagawa · Amami Kato

Abstract Meningeal carcinomatosis (MC) is a refractory disease with a dismal prognosis, and no therapeutic strategy has been established to date. Herein we report a case of lung adenocarcinoma-derived MC in which the patient's performance status was dramatically improved by administration of gefitinib suspension via a nasogastric tube. The patient was a 71-year-old woman who was originally admitted to our hospital for a progressive headache and subsequently presented with severe consciousness disturbance. Cerebrospinal fluid examination and systemic imaging studies revealed MC that was derived from lung adenocarcinoma. Moreover, epidermal growth factor receptor (*EGFR*) mutations were detected in the tumor cells. Since the patient suffered from hydrocephalus, a ventriculoperitoneal shunt was placed. Nevertheless, her consciousness disturbance persisted. Subsequently, gefitinib suspension was prepared and administered via nasogastric tube, which dramatically improved her consciousness level and enabled her to tolerate oral intake. She died 14 months after the disease onset. The observations in this case report suggest that gefitinib might be a therapeutic option for patients with MC derived from cancers harboring *EGFR* mutations even though the patient exhibited severe consciousness disturbance.

Introduction

Meningeal carcinomatosis (MC) is a refractory disease with a dismal prognosis that occurs in 5–10 % of cancer patients [1]. No therapeutic strategy has been established to date; the median survival time is 4–6 weeks if the disease is left untreated [1]. On the other hand, the recent development of novel chemotherapies has markedly improved the outcome of advanced cancer patients. The advent of molecular-targeted drugs is the most prominent among them, and gefitinib is a representative drug for lung cancer. Gefitinib has been shown to prolong the progression-free survival of patients with lung cancer harboring epidermal growth factor receptor (*EGFR*) mutations compared with standard chemotherapy [2, 3]. However, gefitinib is supplied in a tablet form and therefore needs to be administered orally. For this reason, patients with brain metastasis and/or MC sometimes have difficulty tolerating standard gefitinib treatment because they frequently exhibit consciousness disturbance and/or swallowing difficulty. Herein we report a case of lung adenocarcinoma-derived MC in which the patient's performance status (PS) was dramatically improved by administration of gefitinib suspension via a nasogastric (NG) tube even though the patient exhibited severe consciousness disturbance.

T. Okuda (✉) · H. Yoshioka · T. Tasaki · A. Kato
Department of Neurosurgery, Kinki University Faculty
of Medicine, 377-2 Ohno-Higashi, Osaka-Sayama,
Osaka 589-8511, Japan
e-mail: okuda@med.kindai.ac.jp

H. Hayashi · K. Nakagawa
Department of Medical Oncology, Kinki University
Faculty of Medicine, Osaka, Japan

M. Fujita
Department of Microbiology, Kinki University
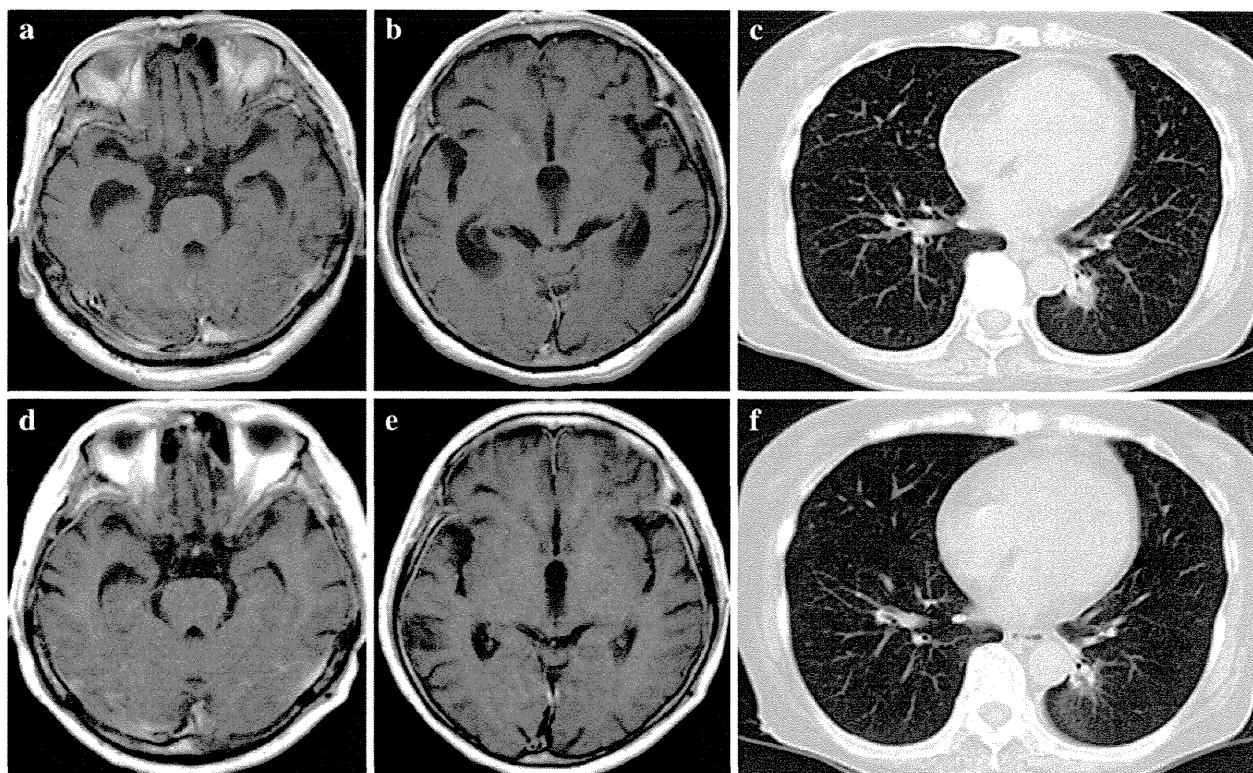Faculty of Medicine, Osaka, Japan

🙋 Springer

Fig. 1 Imaging studies pre- and post-gefitinib treatment. **a, b** T1-weighted gadolinium-enhanced MRI of the head reveals multiple small enhanced lesions. **c** Chest CT shows a mass-like lesion in the left lung S6 with diffuse granular shadows. **d, e** T1-weighted gadolinium-enhanced MRI reveals complete disappearance of the enhanced lesions. **f** Chest CT shows a decrease in size of the primary lesion

Case report

The patient was a 71-year-old woman who suffered from a progressive headache that had lasted several weeks. She suddenly presented with consciousness disturbance and was emergently admitted to our hospital. At the time of admission, her consciousness level was lethargic. Her past medical history was unremarkable. Magnetic resonance images (MRI) of the head revealed multiple small enhanced lesions and hydrocephalus (Fig. 1a, b). Cerebrospinal fluid (CSF) examination showed a cell count of 18/3 mm^3, protein 44 mg/dl, glucose 42 mg/dl, and carcinoembryonic antigen (CEA) 54.4 ng/ml (serum CEA 13.5 ng/ml). Adenocarcinoma cells were detected in the CSF. At the same time, computed tomography (CT) revealed a mass-like lesion in the left lung S6 segment along with diffuse granular shadows (Fig. 1c). These findings led us to diagnose MC that was derived from lung adenocarcinoma (cT1N0M1). *EGFR* mutations were also detected in exon 19 in the tumor cells, which was considered an appropriate target of gefitinib treatment.

Figure 2 shows the clinical course of the patient after the admission. The patient's consciousness level needed to recover for her to receive standard gefitinib treatment orally. Therefore we decided to place a ventriculoperitoneal (VP) shunt to treat the hydrocephalus. Nevertheless, the VP shunt failed to improve her consciousness level. Then, we sought to administer gefitinib suspension to the patient via an NG tube. Gefitinib tablets were finely crushed and suspended in 50 ml of sterile water (Fig. 3), and the patient received 250 mg/day gefitinib via an NG tube. On day 10 after the initiation of gefitinib treatment, her consciousness level improved dramatically, and she was able to tolerate oral intake on the following day. The imaging findings concurrently improved on the follow-up MRIs and CT (Fig. 1d–f). CSF cytology turned out to be negative on day 28. At the same time, CEA levels in the CSF also decreased to 11.3 ng/ml (serum CEA 11.8 ng/ml). The patient recovered with no neurological deficits and no adverse reactions. Gefitinib treatment was continued orally, and the patient was transferred for rehabilitation on day 82. She died 14 months after the disease onset without the cause of death identified.

Fig. 2 Clinical course of the MC patient. *KPS* Karnofsky performance status, *CSF* cerebrospinal fluid, *CEA* carcinoembryonic antigen
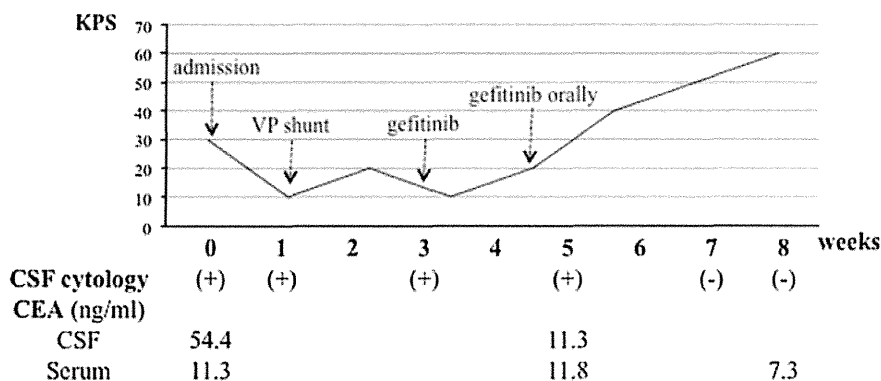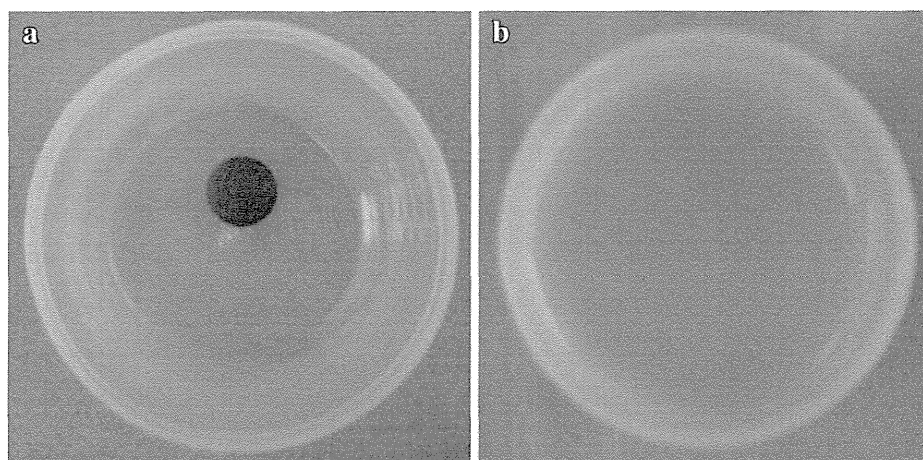

CSF cytology	(+)	(+)		(+)		(+)		(-)	(-)	
CEA (ng/ml)										
CSF	54.4					11.3				
Serum	11.3					11.8			7.3	

Fig. 3 Gefitinib processing for trans-NG tube administration. **a** Original gefitinib tablet. **b** Suspension of gefitinib in sterile water

Discussion

First-line gefitinib has been shown to improve the outcome of poor PS patients with *EGFR* mutation-positive lung cancers [4]. Therefore, examination of EGFR mutation as a biomarker is recommended in this patient population. However, since gefitinib is supplied in a tablet form and usually administered orally, standard gefitinib treatment is sometimes difficult for those with brain metastasis and/or MC because they frequently exhibit consciousness disturbance and/or swallowing difficulties. To treat these patients harboring *EGFR* mutations, gefitinib can be used in suspension by partially breaking the film coating and adding water [5]. Of note, the tablet film coating is not intended to enable sustained release or provide an enteric coating. Furthermore, administration of gefitinib suspension is comparable to administration of tablets in terms of bio-availability and safety [5]. On the basis of these findings, we postulated that the gefitinib suspension could provide the same therapeutic effect in this patient as the gefitinib tablets. Indeed, this therapeutic strategy successfully improved the patient's PS even though she had exhibited severe consciousness disturbance.

Although gefitinib is a small molecule inhibitor, intrathecal transfer rate is generally very low [6]. Particularly in MC patients, the concentration of gefitinib in the CSF has been reported as less than 1 % of the serum concentration [7, 8]. Nevertheless, the administration of gefitinib suspension improved the patient's PS in this case. We speculate several reasons for this. One is that even a low concentration of gefitinib would be effective against *EGFR* mutation-positive MC. Another reason is that the MC would destroy the blood–brain barrier (BBB) in situ and accelerate the drug transfer to each lesion. Indeed, whole-brain irradiation has been shown to enhance the intrathecal delivery of gefitinib by disruption of the BBB [9].

Erlotinib has been shown to induce higher bioactivities in plasma than gefitinib at similar or even lower doses of administration [10]. In addition, intrathecal gefitinib/erlotinib concentration can be elevated in a dose-escalating manner [7]. These findings suggest that erlotinib can be an alternative option for patients with MC or brain metastases if the primary cancer cells harbor *EGFR* gene mutations. We are currently in the process of determining the therapeutic efficacy of erlotinib for those with brain metastases harboring *EGFR* mutations.

A remaining issue is drug resistance exhibited by cancers. In the case of gefitinib/erlotinib, this typically occurs 8–12 months from the initiation of treatment. Over 50 % of resistance is caused by a mutation in the ATP binding pocket of the EGFR kinase domain involving substitution of a small polar threonine residue with a large nonpolar methionine residue (T790M) [11, 12]. In this regard, commencing treatment with a number of different therapeutic agents with differing modes of action is proposed to overcome the development of T790M and other resistance-conferring mutations [13].

In conclusion, we have reported the case of lung adenocarcinoma-derived MC in which the patient's PS was dramatically improved by the administration of gefitinib via an NG tube. The observations in this case report suggest that gefitinib/erlotinib might be therapeutic options for patients with MC derived from cancers harboring *EGFR* mutations even for the patients exhibiting severe consciousness disturbance.

Conflict of interest The authors declare that we have no conflict of interest.

References

1. Leal T, Chang JE, Mehta M et al (2011) Leptomeningeal metastasis: challenges in diagnosis and treatment. Curr Cancer Ther Rev 7:319–327
2. Maemondo M, Inoue A et al (2010) Gefitinib or chemotherapy for non-small-cell lung cancer with mutated EGFR. N Engl J Med 362:2380–2388
3. Mitsudomi T, Morita S, Yatabe Y et al (2010) Gefitinib versus cisplatin plus docetaxel in patients with non-small-cell lung cancer harbouring mutations of the epidermal growth factor receptor (WJTOG3405): an open label, randomised phase 3 trial. Lancet Oncol 11:121–128
4. Inoue A, Kobayashi K, Usui K et al (2009) First-line gefitinib for patients with advanced non-small-cell lung cancer harboring epidermal growth factor receptor mutations without indication for chemotherapy. J Clin Oncol 27:1394–1400
5. Cantarini MV, McFarquhar T, Smith RP et al (2004) Relative bioavailability and safety profile of gefitinib administered as a tablet or as a dispersion preparation via drink or nasogastric tube: results of a randomized, open-label, three-period crossover study in healthy volunteers. Clin Ther 26:1630–1636
6. Togashi Y, Masago K, Masuda S et al (2012) Cerebrospinal fluid concentration of gefitinib and erlotinib in patients with non-small cell lung cancer. Cancer Chemother Pharmacol 70:399–405
7. Jackman DM, Holmes AJ, Lindeman N et al (2006) Response and resistance in a non-small-cell lung cancer patient with an epidermal growth factor receptor mutation and leptomeningeal metastases treated with high-dose gefitinib. J Clin Oncol 24:4517–4520
8. Fukuhara T, Saijo Y, Sakakibara T et al (2008) Successful treatment of carcinomatous meningitis with gefitinib in a patient with lung adenocarcinoma harboring a mutated EGF receptor gene. Tohoku J Exp Med 214:359–363
9. Stemmler HJ, Schmitt M, Willems A et al (2007) Ratio of trastuzumab levels in serum and cerebrospinal fluid is altered in HER2-positive breast cancer patients with brain metastases and impairment of blood–brain barrier. Anticancer Drugs 18:23–28
10. Karaman MW, Herrgard S, Treiber DK et al (2008) A quantitative analysis of kinase inhibitor selectivity. Nat Biotechnol 26:127–132
11. Pao W, Miller VA, Politi KA et al (2005) Acquired resistance of lung adenocarcinomas to gefitinib or erlotinib is associated with a second mutation in the EGFR kinase domain. PLoS Med 2:e73
12. Yun CH, Mengwasser KE, Toms AV et al (2008) The T790M mutation in EGFR kinase causes drug resistance by increasing the affinity for ATP. Proc Natl Acad Sci U S A 105:2070–2075
13. Tang Z, Du R, Jiang S et al (2008) Dual MET-EGFR combinatorial inhibition against T790M-EGFR-mediated erlotinib-resistant lung cancer. Br J Cancer 99:911–922

Surgical Treatment for Multiple Brain Metastases

Takeshi Okuda and Amami Kato

Additional information is available at the end of the chapter

http://dx.doi.org/10.5772/52353

1. Introduction

Brain metastasis occurs with a fairly high frequency, in 25–35% of cancer patients [1]. Because brain metastasis directly affects prognosis, quality of life (QOL), and performance status (PS), treatment is crucial. Survival time is reported to be 1 month in the case of untreated brain metastasis [2], 2 months with steroid treatment alone [3], and 3-6 months with whole-brain radiotherapy (WBRT) [4-7]. This shows that brain metastasis is a seriously life-threatening condition. Therapeutic approaches have become more varied with the appearance of stereotactic radiosurgery (SRS), and establishment of multiple treatment plans has become possible. In addition to surgical resection (SR), WBRT, and SRS, systemic chemotherapy (SC) is also an option. The ideal treatment is to control the brain metastasis and prevent destruction of the central nervous system using combinations of these therapeutic approaches. Among these multiple approaches, SR is effective in that it enables treatment of large tumors and early improvement of symptoms, which are not possible with other approaches. The indications for SR are expanded with the early improvement of symptoms, leading particularly to improved QOL from the palliative viewpoint. However, SR is also highly invasive compared with other treatments, and the indications are strict. The standard surgical indication is single brain metastasis, and patients with fairly good prognosis, such as those with good general condition, are selected [8]. Recently, however, partly as a result of advances in imaging, the number of cases of multiple brain metastases has been trending upward. This means that there are patients in whom SR is excluded as an indication because of findings for multiple brain metastases, and who cannot obtain the benefits of surgery. We provide aggressive treatment using the same surgical indications for cases of multiple brain metastases as for single metastasis. The present study therefore investigated treatment outcomes and reported on the effectiveness of SR for multiple brain metastases.

2. Methods

Subjects were 100 patients with brain metastasis who underwent craniotomy and surgical removal of tumors in the Department of Neurosurgery at Kinki University Hospital between 2004 and 2011. They included 54 patients with single brain metastasis and 46 with multiple brain metastases. Details are shown in Table 1.

Characteristic	Single	Multiple
No. of cases	54	46
Age (mean)	63.3	61.3
Range	39-81	46-81
Male-to-female ratio	31:23	22:24
Primary site		
Lung	29	22
Breast	9	13
Rectum	2	3
Colon	3	1
Kidney	2	1
Other	9	6
RPA classification		
I	18	10
II	21	12
III	15	24
Size (mm, mean)	34.1	28.7

Table 1. Clinical characteristics of patients with single and multiple brain metastases

Surgical indications are shown in Figure 1, and treatments following surgery were done in close conference with departments related to cancer, such as the Department of Radiation Oncology and the Department of Medical Oncology. Each case was treated using a tailor-made approach.
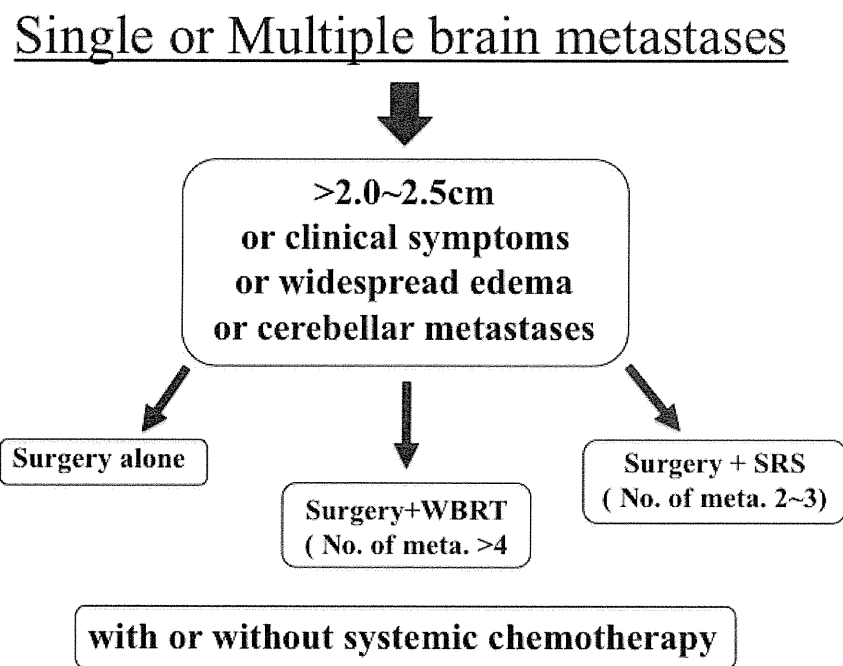
Single or Multiple brain metastases

⬇

> 2.0~2.5cm
or clinical symptoms
or widespread edema
or cerebellar metastases

Surgery alone

**Surgery+WBRT
(No. of meta. >4**

**Surgery + SRS
(No. of meta. 2~3)**

with or without systemic chemotherapy

Figure 1. Therapeutic strategies in brain metastases

The basic surgery was en bloc resection, with resection of a single site even in cases of multiple metastases. During removal, we used fluorescence-guided surgery using fluorescein sodium with transformation to a solid-type tumor by hydrofiber dressing for cystic lesions [9-11]. In comparing survival time, duration of survival from the day of surgery until death was obtained using the Kaplan-Meier method, and significant differences were determined with the log-rank test. For all tests, a significance level of 5% was applied.

3. Results

Among the 100 patients, gross total resection was performed in 89%. Reasons for sub-total resection were invasion into blood vessels or dura mater, huge tumor size, or tumor involving an eloquent area. Follow-up treatments are shown in Figure 2. SC was also performed in 45 cases.
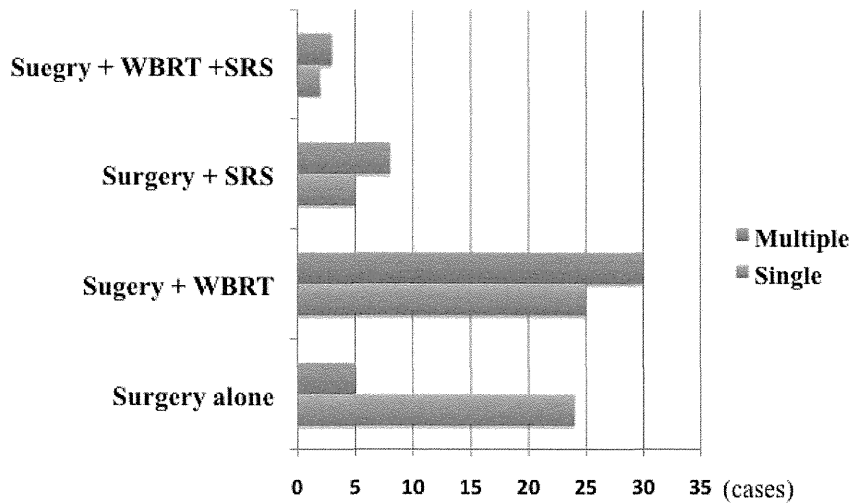

Figure 2. Postoperative treatments. Concurrent systematic chemotherapy was used in 45% of cases.

Central nervous system death occurred in 9% and 6 patients died within 3 months of surgery. Three of these patients showed exacerbation of the primary cancer and three showed poor control of brain metastases. For all 100 patients median survival time (MST) was 9.3 months, the 1-year survival rate was 45%, the 2-year survival rate was 10%. A comparison of single and multiple metastases is shown in Table 2.

	Single	Multiple
Median survival time (mo)	9.8	8.1
1-year survival rate (%)	44	46
2-year survival rate (%)	11	9

Table 2. Survival rate of single and multiple metastases

In this comparison by number of metastases, no significant differences were seen in survival time, including 1-year survival rate, 2-year survival rate, or MST (Fig. 3).
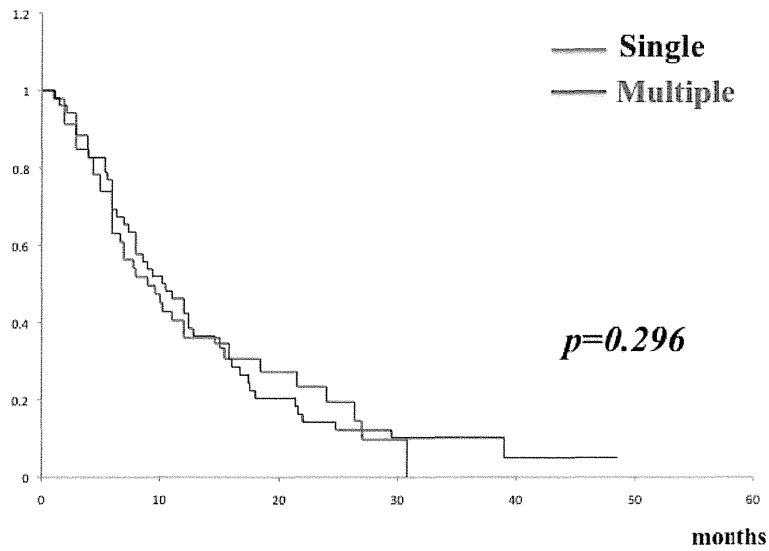
Figure 3. Comparison of survival times with single and multiple brain metastases. No statistically significant difference was confirmed between the 2 groups (p=0.296).

In a comparison by number of metastases in patients with multiple metastases, no significant difference in survival time was seen between patients with 2-3 metastases (MST, 8.8 months; n=32) and those with ≥4 metastases (MST, 8.0 months; n=14) (Fig. 4).
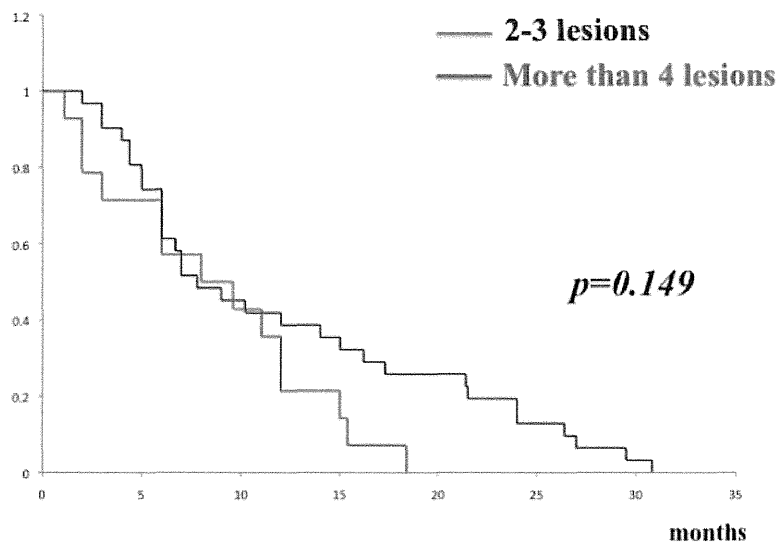

Figure 4. Comparison of survival times according to number of metastases in cases of multiple brain metastases. No statistically significant difference was confirmed between the 2 groups (p=0.149).

In addition, new pathological findings were revealed through pathological diagnosis obtained with SR, and the treatment strategy was changed in some cases. The case of a typical patient is described below.

This patient was a 49-year-old woman who was undergoing chemotherapy for lung cancer (adenocarcinoma). SC was continued for 4 courses, when she was switched to best supportive care because of a lack of efficacy. In screening tests for headache and visual impairment, six brain metastases were seen. At this point, multiple metastases to other organs were identified and she was expected to live less than 3 months (Fig. 5A-C).
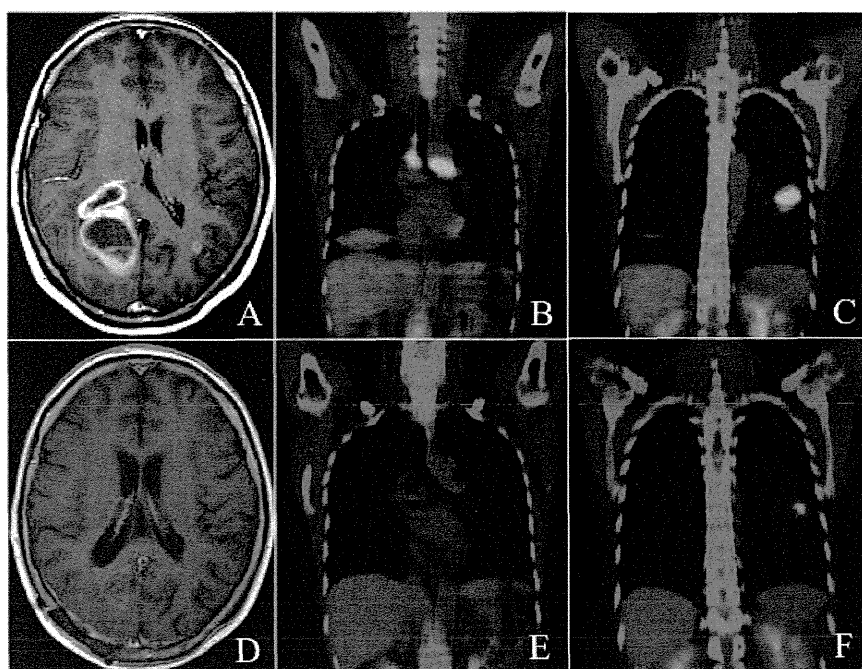

Figure 5. A) Contrast-enhanced MRI findings before treatment. A total of six metastases are seen, including a lesion ≥4 cm in diameter with ventricular invasion in the right occipital lobe. (B,C) Preoperative FDG-PET examination. Multiple metastases are seen in the lungs. (D) Contrast-enhanced MRI after treatment. All of the multiple lesions have disappeared. (E,F) FDG-PET examination following systemic chemotherapy. The lesions in the lungs are markedly reduced in size.

Headache associated with increased intracranial pressure is difficult to treat, and SR was performed for the right occipital lobe lesion with the aim of relieving symptoms. Symptoms rapidly improved after surgery, and the pathological diagnosis was small cell cancer. Initially, the diagnosis had been adenocarcinoma based on adenocarcinomatous tissue obtained from bronchoscopic biopsy of the primary lung cancer. In fact, however, the tumor represented mixed-type lung cancer with small cell cancer, and these brain metastases was thought to represent a recurrence of the small cell cancer. WBRT was performed postoperatively and SC

was applied using the approach used for small cell lung cancer. A marked decrease in systemic lesions was seen (Fig. 5D-F). Ultimately, the patient survived 19 months after surgery. This patient obtained a greater-than-expected benefit from surgery.

4. Discussion

Various biases are inherent in the treatment for brain metastasis, according to factors such as the primary cancer or general condition. Moreover, because of the problem of brain function, establishing a treatment plan can be difficult. In such circumstances, many reports with a fairly high evidence level have described results for single brain metastasis. Reports on level I include those of Patchell et al. [12] and Noordijk et al. [13] in the 1990s. SR + WBRT was established for single brain metastasis based on these reports. In a report by Bindal et al. [14], SR for multiple brain metastases was seen to be effective only in cases when all of the multiple brain metastases could be removed. However, when all lesions could not be removed, no significant difference was seen compared with WBRT alone, and SR was not considered effective. Based on these findings, the priority came to be placed on WBRT monotherapy in cases of multiple brain metastases, but treatment later diversified with active SRS intervention for brain metastasis and in 1999 Kondziolka et al. [15] reported WBRT + SRS combination radiotherapy for cases of multiple brain metastasis. With this approach, significantly longer survival times were obtained compared with WBRT alone, and WBRT + SRS became the general therapy for multiple brain metastases. In 2006, Aoyama et al. [16] also reported the efficacy of SRS monotherapy for brain metastasis with ≤4 lesions. Various treatment strategies have thus been reported, including not only conventional WBRT, but also combination with SRS and SRS monotherapy. Recent reports have also suggested the efficacy of SC for multiple brain metastases [17]. Up to this time, there has been little recognition of the efficacy of SC for brain metastasis. A response rate of 60% has been reported, but the effect is temporary and MST is less than 6 months in the majority of cases [18-20]. However, striking advances have recently been made in SC, with the emergence of molecularly targeted drugs as a major breakthrough. Drugs for lung cancer include gefitinib and erlotinib. The response rate to erlotinib is in cases of brain metastasis with EGFR mutation, showing very high efficacy. In breast cancer, the appearance of lapatinib is also reported to be effective against brain metastasis. SC will thus likely become necessary as one therapeutic approach in brain metastasis, particularly for patients with multiple brain metastases.

As mentioned above, various therapeutic approaches can be used for brain metastasis, including SR, WBRT, SRS, and SC, and various combinations. In this situation, at our hospital, we do not consider it necessary to select treatment based on the number of metastases, such as single or multiple, and aggressively perform SR in cases of multiple metastases just as in cases of single metastasis. Likewise in follow-up treatment, we implement tailor-made treatment strategies matched to the individual patients. The results have shown no differences in either MST or survival rate depending on the number of metastases, and good treatment outcomes have been obtained in cases of multiple brain metastases. Today, when various therapeutic approaches are available, performing SR to eliminate lesions at an early stage is

highly effective. Early improvement of symptoms leads to improved PS and QOL, producing new treatment opportunities. In addition, early elimination of brain metastatic lesions reduces the steroid dosage as well as the possibility of radiation necrosis. The result is thought to lead ultimately to longer survival times. In our investigation, prognosis tended to be better for the group with fewer brain metastases (2-3 lesions), but the difference did not reach the level of statistical significance. This suggests that there is no correlation between prognosis and the number of metastases, including even single brain metastases. This is also supported by the low probability of central nervous system death. The total number of patients in this study was low (100 patients) and it was not a randomized controlled trial, so the results of evaluation are not definitive. However, the advances in cancer treatment in recent years may necessitate a rethink of the policy of determining treatment plans based on the number of metastases.

5. Conclusions

The efficacy of SR in multiple brain metastases was investigated. Survival time and survival rate were not significantly different compared with single brain metastasis, and no significant difference was seen in a comparison of survival time according to number of metastases. The reasons are thought to be that tailor-made therapeutic strategies using the multimodalities advanced in recent years are effective. It may be time to rethink the approach of determining treatment plans based on the number of metastases in therapeutic strategies for brain metastases.

Author details

Takeshi Okuda and Amami Kato

*Address all correspondence to: okuda@neuro-s.med.kindai.ac.jp

Department of Neurosurgery, Kinki University School of Medicine, Osaka, Japan

References

[1] Paek SH, Audu PB, Sperling MR, Cho J, Andrews DW. Reevaluation of surgery for the treatment of brain metastases: Review of 208 patients with single or multiple brain metastases treated at one institution with modern neurosurgical techniques. Neurosurgery 2005;56: 1021-1034.

[2] Markesbery WR, Brooks WH, Gupta GD, Young AB. Treatment for patients with cerebral metastases. Arch Neurol 1978;35: 754-756.

[3] Ruderman NB, Hall TC. Use of glucocorticoids in the palliative treatment of meta-static brain tumors. Cancer 1965;18: 298-306.

[4] Cairncross JG, Kim JH, Posner JB. Radiation therapy for brain metastases. Ann Neu-rol 1980;7: 529-541.

[5] Kurtz JM, Gelber R, Brady LW, Carella RJ, Cooper JS. The palliation of brain metasta-ses in a favorable patient population: A randomized clinical trial by the Radiation Oncology Group. Int J Radiat Oncol Biol Phys 1981;7: 891-895.

[6] Patchell RA, Tibbs PA, Regine WF, Dempsey RJ, Mohiuddin M, Kryscio RJ, Markesb-ery WR, Foon KA, Young B. Postoperative radiotherapy in the treatment of single metastases to the brain: A randomized trial. JAMA 1998;280: 1485-1489.

[7] Sause WT, Crowley JJ, Morantz R, Rotman M, Mowry PA, Bouzaglou A, Borst JR, Se-lin H. Solitary brain metastasis: Results of an RTOG/SWOG protocol evaluation sur-gery plus RT versus RT alone. Am J Clin Oncol 1990;13: 427-432.

[8] Mut M. Surgical treatment of brain metastasis: A review. Clin Neurol Neurosurg 2012;114(1): 1-8.

[9] Okuda T, Kataoka K, Taneda M. Metastatic brain tumor surgery using fluorescein so-dium: technical note. Minim Invas Neurosurg 2007;50: 382-384.

[10] Okuda T, Teramoto Y, Yugami H, Kataoka K, Kato A. Surgical technique for a cystic-type metastatic brain tumor: transformation to a solid-type tumor using hydrofiber dressing. Surg Neurol 2009;72: 703-706.

[11] Okuda T, Kataoka K, Yabuuchi T, Yugami H, Kato A. Fluorescence-guided surgery of metastatic brain tumors using fluorescein sodium. J Clin Neurosci 2010;17: 118-121.

[12] Patchell RA, Tibbs PA, Walsh JW, Dempsey RJ, Maruyama Y, Kryscio RJ, Markesb-ery WR, Macdonald JS, Young B. A randomized trial of surgery in the treatment of single metastases to the brain. N Engl J Med 1990;322: 494-500.

[13] Noordijk EM, Vecht CJ, Haaxma-Reiche H, Padberg GW, Voormolen JH, Hoekstra FH, Tans JT, Lambooij N, Metsaars JA, Wattendorff AR. The choice of treatment of single brain metastasis shoud be based on extracranial tumor activity and age. Int J Radiat Oncol Biol Phys 1994;29: 711-717.

[14] Bindel RK, Sawaya R, Leavens ME, Lee JJ. Surgical treatment of multiple brain meta-stases. J Neurosurg 1993;79: 210-216.

[15] Kondziolka D, Patel A, Lunsford LD, Kassam A, Flickinger JC. Stereotactic radiosur-gery plus whole brain radiotherapy versus radiotherapy alone for patients with mul-tiple brain metastases. Int J Radiat Oncol Biol Phys 1999;45: 427-434.

[16] Aoyama H, Shirato H, Tago M, Nakagawa K, Toyoda T, Hatano K, Kenjyo M, Oya N, Hirota S, Shioura H, Kunieda E, Inomata T, Hayakawa K, Katoh N, Kobayashi G.